

Very metal-poor stars in the solar vicinity: age determination

ANASTASHIA PLOTNIKOVA,¹ GIOVANNI CARRARO,¹ SANDRO VILLANOVA,² AND SERGIO ORTOLANI¹

¹*Dipartimento di Fisica e Astronomia, Università di Padova, I-35122, Padova, Italy*

²*Departamento de Astronomía, Casilla 160-C, Universidad de Concepción, Concepción. Chile*

ABSTRACT

The ages of the oldest and most metal-poor stars in the Milky Way bear important information on the age of the Universe and its standard model. We analyze a sample of 28 extremely metal-poor field stars in the solar vicinity culled from the literature and carefully determine their ages. To this aim, we critically make use of Gaia data to derive their distances and associated uncertainties. Particular attention has been paid to the estimate of the reddening and its effect on the derivation of stellar ages. We employed different reddenings and super-impose isochrones from different sources in the stars color-magnitude diagram built up with different photometric systems. We highlight subtle metallicity effects when using the Johnson photometry for low metallicity stars and finally adopt Gaia photometry. An automatic fitting method is devised to assign ages to each individual star taking into account the uncertainties in the input parameters. The mean age of the sample turns out to be 13.9 ± 0.5 Gyr using Padova isochrones, and 13.7 ± 0.4 Gyr using BASTI isochrones. We found also a group of very metal-poor stars ($[F_e/H]$: $-2.7 - -2.0$ dex) with relatively young ages, in the range 8 – 10 Gyr.

Keywords: Milky Way Disk (1050) — Metallicity (1031) — Stellar ages (1581) — Field stars (2103)

1. INTRODUCTION

Stars with extremely low metal abundance are of particular astrophysical and cosmological interest because they probe very early times in the evolution of the Universe and its Galactic components. Through the investigation of the age and chemical composition, we can obtain important constraints on the evolution of the Milky Way, set up a lower limit to the age of the Universe (Bond et al. (2013), VandenBerg et al. (2014)), and understand the chemical properties of the first Population III supernovae in the nascent Milky Way (Frebel & Norris (2015)).

Over the years, several spectroscopic campaigns have been conducted to study the chemical composition of very metal-poor stars (Christlieb et al. (2004), Cayrel et al. (2004), Barklem et al. (2005), Schlaufman & Casey (2014), Limberg et al. (2021), etc.). The most recent investigations of the age of metal-poor stars (Bonaca et al. (2020), Carter et al. (2021)) showed that they are on average old (12.0 ± 1.5 Gyr for turnoff stars). However, both authors discovered the presence of very metal-poor stars with relatively young ages 8 - 10 Gyr (3 stars in Bonaca et al. (2020), 1 star in Carter et al. (2021)).

The current best estimate of the age of the Universe is 13.77 ± 0.06 Gyr, based on the latest WMAP derivation (Bennett et al. (2013)), and it is in excellent agreement with observations of the cosmic microwave background (CMB) using the Planck satellite (Ade et al. (2014)). Recent simulations (e.g., Ritter et al. (2012), Safranek-Shrader et al. (2014)) suggest that the oldest Population II stars probably formed $\sim 0.2 - 0.3$ Gyr after the Big Bang, depending on how quickly the gas from the first (Population III) supernovae was able to cool down and condense, as well as on the relevance and impact of the Population III stellar feedback. Precise ages for the oldest and most metal-poor stars can date the onset of star formation (e.g., Bromm & Larson (2004)) following the Big Bang. Since the oldest stars must be younger than the Universe, precise ages provide a strong test of the consistency between cosmological and stellar physics.

Moreover, the derived age together with high precision spectroscopic measurements of metallicity can help us to reconstruct the age-metallicity relation (AMR) - one of the main observational constraints for any Milky Way formation and evolution model. The first AMR in the solar neighborhood was obtained by Twarog (1980) and it shows an average decrease of the metallicity with the age. Twarog (1980) concluded that the AMR can be used to estimate the star

formation rate via comparison with theoretical models. That means that the AMR is an important tracer of the star formation history of galaxies. An extension of the AMR to the very metal-poor tail will help to understand the early stages of star formation in the Milky Way and in the Universe.

On the other hand, the wide distribution in metallicity in the solar neighborhood, at any given age, suggests that stars have been moving away from their birth locations over time (radial migration) (Grenon (1972), Grenon (1989)). The main mechanisms of radial migration are: transient spiral modes mostly at the co-rotation resonance (Sellwood & Binney (2002)), and non-axisymmetric perturbations to the potential such as bars or galaxy interactions (Bird et al. (2012), Roškar et al. (2008), Quillen et al. (2009)).

A recent intriguing finding, described in Feuillet et al. (2018), is that the youngest stars are not the most metal-rich as previously expected from pure gas enrichment processes. There are two possible reasons for such an occurrence: 1) two modes of star formation, where part of the metal-rich gas is diluted to form stars that are subsequently more metal-poor, or 2) migration of the old, metal-rich stars from the inner to the outer regions of the Galaxy. That means that non-linear patterns in AMR are correlated with the specific events in star formation and dynamical evolution of the Galaxy.

In this study, ages and chemical compositions of a sample of very metal-poor stars are investigated. Our main goal is to compare them with the age of the Universe (13.77 ± 0.06 Gyr) based on data on the CMB, baryon acoustic oscillations, and Hubble constant (Bennett et al. (2013)). We also investigate the chemical composition of these stars to retrieve information about the first Population III supernovae, the chemical composition of the nascent Milky Way, and the AMR behavior in the very metal-poor regime.

2. DATA

As the main target of our research, we used metal-poor stars from the Hamburg vs. ESO R-process Enhanced Star (HERES) survey, spectroscopically studied by Barklem et al. (2005). Their snapshot spectra cover a wavelength range of 3760 - 4980 Å and have an average signal-to-noise ratio of $S/N \sim 54$ per pixel over the entire spectral range. A 2'' slit is employed giving a minimum resolving power of $R \approx 20000$. From the "snapshot" spectra the elemental abundances of moderate precision (absolute rms errors of order 0.25 dex, relative rms errors of order 0.15 dex) have been obtained for 22 elements: C, Mg, Al, Ca, Sc, Ti, V, Cr, Mn, Fe, Co, Ni, Zn, Sr, Y, Zr, Ba, La, Ce, Nd, Sm, and Eu.

We chose this particular data set because of its careful and detailed chemical analysis. It is indeed a unique data set under this point of view. Besides, all stars in the data set under investigation are very metal-poor and this gives us the real opportunity to study the very beginning of the formation and evolution of our Galaxy. Additionally, we wanted to test the cosmological age of the Universe and very metal-poor stars are the best candidates for this purpose.

The final sample of stars analysed in Barklem et al. (2005) contains 253 stars built up with the following criteria:

- No strong molecular carbon features in spectra.
- Metallicity cut-off: $[Fe/H] < -1.5$
- Temperature cut-off: $T_{eff} > 4200$ K
- No spectroscopic binaries or rotators

We complemented spectroscopic data with Gaia (G, G_{BP} , G_{RP}) and Johnson (B, V, I) photometry obtained from the Gaia archive¹ and SIMBAD catalog². The distribution in the galactic plane is shown in Fig.1. Out of these 253 stars only 28 were TO stars for which we could measure good ages (see Section 9). Coordinates, photometry, interstellar absorption, distance, temperature and chemical abundances of these 28 stars are presented in Tab.1. See Sections 4 and 5 for interstellar absorption and distance determination. The main characteristics of the data set:

- Location in the space: Galactic Halo $|b| > 20^\circ$.
- Most of the stars have magnitudes in the range $12 < G < 17$.
- Distance (estimated using Gaia Data Release 3 parallaxes) in the range $0 < d < 30$ kpc.

¹ <https://gea.esac.esa.int/archive/>

² <http://simbad.u-strasbg.fr/simbad/sim-fbasic>

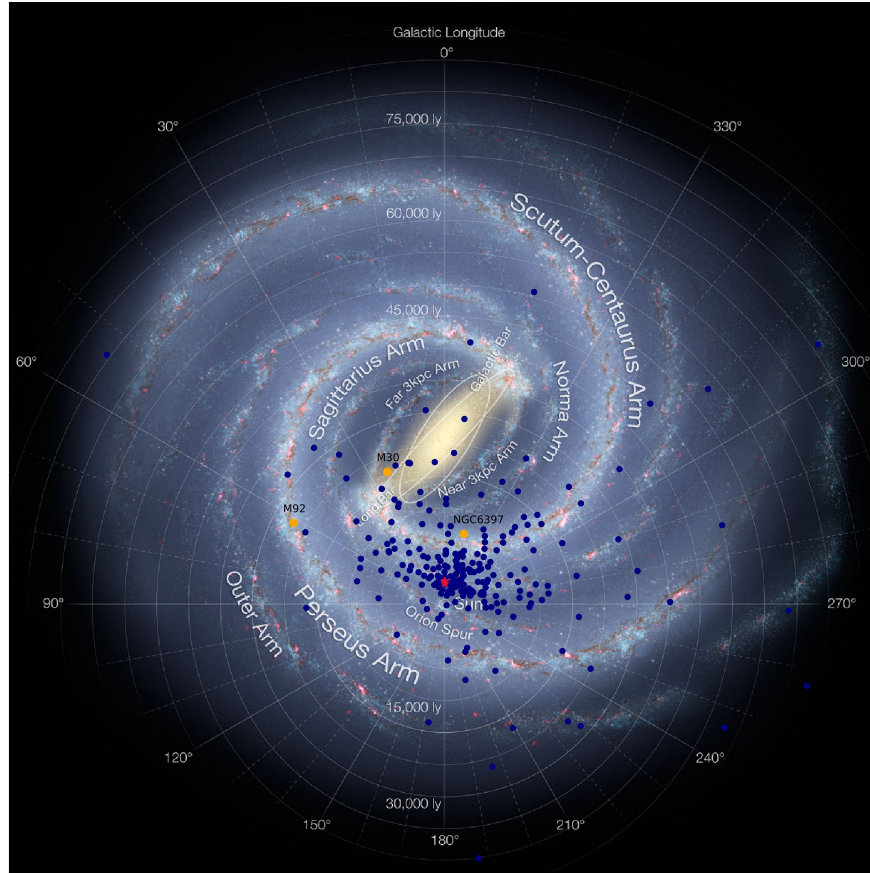


Figure 1. Location of 253 very metal-poor stars (blue) in Galactic plane. Yellow dots are metal-poor globular clusters: NGC 6397, M 30, M 92. Red stars are stars: HD 84937, HD 132475, and HD 140283 (VandenBerg et al. (2014))

- Metallicity in the range $-3.8 < [Fe/H] < 1.5$ dex.
- All stars are α -element enhanced.
- All targets are single stars. Spectroscopic binaries were already removed by Barklem et al. (2005). We checked, however, El-Badry et al. (2021) for spatially resolved binaries. No overlap was found.

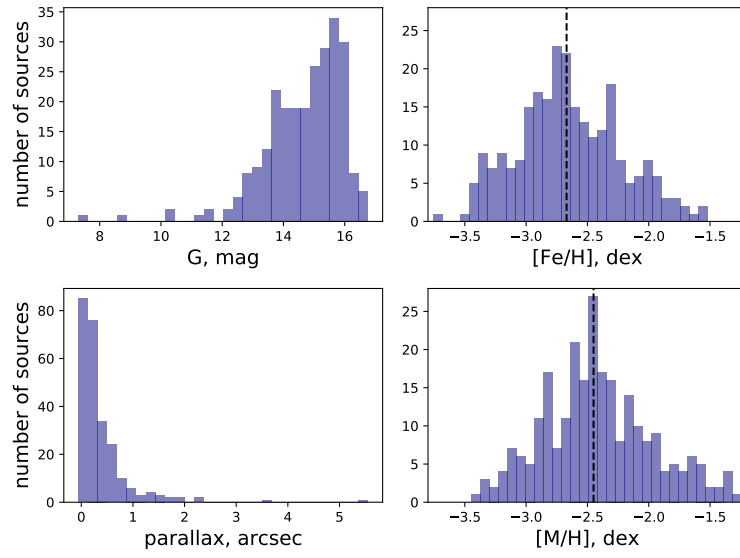


Figure 2. Distribution of very metal-poor stars in G-band (Gaia DR3) - *top left*, in parallax Gaia DR3 - *bottom left*, in total metallicity *top right*, in metallicity - *bottom right*, vertical dashed line is the metallicity mean.

Table 1. Parameters for the stars analyzed in this study.

| ID | RA J2000 | DEC J2000 | B mag | V mag | I mag | G mag | G _{BP} mag | G _{RP} mag | A _V mag | d pc | T _{eff} K | [Fe/H] dex | [C/Fe] dex | |
|--------------|-------------|--------------|----------|----------|----------|----------|------------------------|------------------------|-----------------------|---------|-----------------------|---------------|---------------|------|
| HE_0023-4825 | 00 25 50.31 | -48 08 27.01 | 14.298 | 13.830 | 13.161 | 13.667 | 13.945 | 13.218 | 0.032 | 1164 | 5816 | ... | 2.06 | 0.31 |
| HE_0109-3711 | 01 11 38.40 | -36 55 17.11 | 16.668 | 16.290 | 15.691 | 16.160 | 16.400 | 15.757 | 0.025 | 3662 | 6156 | ... | 1.91 | 0.31 |
| HE_0231-4016 | 02 33 44.39 | -40 03 42.72 | 16.494 | 16.090 | 15.475 | 15.939 | 16.185 | 15.532 | 0.036 | 2634 | 5972 | ... | 2.08 | 1.36 |
| HE_0340-3430 | 03 42 04.76 | -34 20 50.10 | ... | 14.783 | 14.189 | 14.657 | 14.910 | 14.238 | 0.031 | 1780 | 5914 | ... | 1.95 | 0.06 |
| HE_0430-4404 | 04 31 38.10 | -43 57 48.71 | ... | 15.724 | 15.166 | 15.629 | 15.868 | 15.236 | 0.035 | 1569 | 6214 | ... | 2.07 | 1.44 |
| HE_0447-4858 | 04 49 01.00 | -48 53 36.15 | 16.687 | 16.254 | 15.624 | 16.140 | 16.398 | 15.727 | 0.038 | 3261 | 5995 | ... | 1.69 | 0.04 |
| HE_0501-5139 | 05 02 48.21 | -51 35 36.30 | 16.573 | 16.094 | 15.475 | 15.980 | 16.250 | 15.543 | 0.059 | 4539 | 5861 | ... | 2.38 | 0.40 |
| HE_0519-5525 | 05 19 59.15 | -55 22 41.81 | 15.570 | 15.034 | 14.284 | 14.862 | 15.171 | 14.374 | 0.066 | 2376 | 5580 | ... | 2.52 | 0.29 |
| HE_0534-4615 | 05 35 52.94 | -46 13 35.97 | ... | 15.056 | 14.317 | 14.896 | 15.231 | 14.382 | 0.062 | 2266 | 5506 | ... | 2.01 | 0.13 |
| HE_0938+0114 | 09 40 43.20 | +01 00 29.51 | ... | ... | ... | 10.344 | 10.560 | 9.964 | 0.034 | 180 | 6777 | ... | 2.51 | 0.65 |
| HE_1052-2548 | 10 55 20.53 | -26 04 48.03 | 13.492 | 13.188 | 12.541 | 13.115 | 13.364 | 12.699 | 0.127 | 675 | 6534 | ... | 2.29 | 0.51 |
| HE_1105+0027 | 11 07 49.50 | +00 11 38.34 | 16.038 | 15.646 | 15.018 | 15.594 | 15.852 | 15.166 | 0.005 | 3162 | 6132 | ... | 2.42 | 2.00 |
| HE_1225-0515 | 12 28 12.42 | -05 31 40.63 | ... | 15.584 | 14.947 | 15.524 | 15.767 | 15.118 | 0.005 | 2410 | 6210 | ... | 1.96 | 0.52 |
| HE_1330-0354 | 13 33 10.67 | -04 10 05.80 | 15.248 | 15.000 | 14.380 | 14.937 | 15.169 | 14.537 | 0.082 | 1716 | 6257 | ... | 2.29 | 1.05 |
| HE_2250-2132 | 22 53 40.48 | -21 16 23.96 | 14.905 | 14.392 | 13.662 | 14.220 | 14.526 | 13.735 | 0.027 | 1780 | 5705 | ... | 2.22 | 0.41 |
| HE_2347-1254 | 23 50 10.01 | -12 37 50.46 | 13.839 | 13.358 | 12.779 | 13.248 | 13.499 | 12.833 | 0.064 | 783 | 6132 | ... | 1.83 | 0.27 |
| HE_2347-1448 | 23 49 58.34 | -14 32 15.60 | 15.692 | 15.226 | 14.615 | 15.109 | 15.374 | 14.672 | 0.050 | 3062 | 6162 | ... | 2.31 | 0.50 |
| HE_0244-4111 | 02 45 57.45 | -40 59 06.81 | 15.531 | 15.025 | 14.302 | 14.839 | 15.141 | 14.356 | 0.075 | 2380 | 5624 | ... | 2.56 | 0.25 |
| HE_0441-4343 | 04 43 20.43 | -43 38 20.51 | ... | 15.559 | 14.835 | 15.388 | 15.695 | 14.904 | 0.047 | 3511 | 5629 | ... | 2.52 | 0.33 |
| HE_0513-4557 | 05 15 12.21 | -45 54 10.46 | 16.279 | 15.743 | 15.045 | 15.609 | 15.913 | 15.133 | 0.038 | 3602 | 5629 | ... | 2.79 | 0.39 |
| HE_0926-0508 | 09 28 55.35 | -05 21 40.48 | 12.340 | 12.194 | 11.617 | 12.126 | 12.357 | 11.735 | 0.086 | 457 | 6249 | ... | 2.78 | 0.62 |
| HE_1006-2218 | 10 09 00.69 | -22 33 30.00 | ... | 13.773 | 13.197 | 13.717 | 13.936 | 13.345 | 0.102 | 928 | 6638 | ... | 2.69 | 9.99 |
| HE_1015-0027 | 10 17 35.70 | -00 42 24.30 | 15.621 | 15.342 | 14.701 | 15.271 | 15.519 | 14.846 | 0.145 | 1886 | 6315 | ... | 2.66 | 9.99 |
| HE_1120-0153 | 11 22 43.39 | -02 09 36.69 | 12.210 | 11.789 | 11.036 | 11.646 | 11.884 | 11.242 | 0.110 | 509 | 6191 | ... | 2.77 | 0.63 |
| HE_1126-1735 | 11 28 51.39 | -17 51 42.82 | ... | 15.965 | 15.232 | 15.890 | 16.166 | 15.445 | 0.132 | 4118 | 5689 | ... | 2.69 | 0.23 |
| HE_1413-1954 | 14 16 04.71 | -20 08 54.09 | ... | 15.235 | 14.593 | 15.171 | 15.418 | 14.745 | 0.225 | 1966 | 6533 | ... | 3.22 | 1.45 |
| HE_2222-4156 | 22 25 28.65 | -41 40 57.72 | ... | 15.332 | 14.583 | 15.252 | 15.538 | 14.783 | 0.042 | 2773 | 5537 | ... | 2.73 | 0.42 |
| HE_2325-0755 | 23 27 59.61 | -07 39 13.49 | 14.481 | 13.940 | 13.251 | 14.200 | 14.452 | 13.776 | 0.044 | 1600 | 5665 | ... | 2.85 | 0.21 |

3. ISOCHRONES

To derive age we used two different sets of isochrones for old metal-poor populations: Padova isochrones³ and a Bag of Stellar Tracks and Isochrones⁴ (BaSTI).

We used these two sources of isochrones to check for systematics due to differences in stellar evolution models. For example, Padova isochrones do not take into account α -enhancement while most of the studied stars are α -enhanced. BaSTI isochrones instead have main sequence bluer than references globular clusters (Hidalgo et al. (2018)). We can

³ <http://stev.oapd.inaf.it/cmd>

⁴ <http://basti-iac.oa-abruzzo.inaf.it/isocs.html>

| Parameter | BaSTI | Padova |
|-----------------------|---------------------------------------------------------------|------------------------------------|
| Age | 1 – 15 Gyr with step 0.1 Gyr | 1 – 20 Gyr with step 0.1 Gyr |
| [Fe/H] | ⋯ 1.05, -1.2, -1.3, -1.4, -1.55, -1.7, -1.9, -2.2, -2.5, -3.2 | ⋯ 1.0 – -2.2 dex with step 0.1 dex |
| Heavy element mixture | $[\alpha/\text{Fe}] = +0.4$ | $[\alpha/\text{Fe}] = +0.0$ |
| Photometric system | UBVIJHK, Gaia DR3 | UBVIJHK, Gaia DR3 |

Table 2. Characteristics of the BaSTI and Padova isochrones we used in this study.

| Source | Year | Type of the map | Coverage | Accuracy |
|----------------------------|------|-----------------|-----------------------------------------------------------------|-------------|
| Schlegel et al. | 1998 | 2D | all sky | 16% |
| Schlafly & Finkbeiner | 2011 | 2D | all sky | 50 mmag |
| Queiroz et al. (StarHorse) | 2019 | 3D | $ Z_{Gal} < 1 \text{ kpc}$, $R_{Gal} \lesssim 20 \text{ kpc}$ | 50-200 mmag |
| Green et al. | 2018 | 3D | $\delta \gtrsim -30^\circ$, $d^* \lesssim 60 \text{ kpc}$ | 10-100 mmag |
| Lallement et al. | 2018 | 3D | $D^{**} \leq 4000 \text{ pc}$, $ Z_{Gal} \leq 600 \text{ pc}$ | 10-150 mmag |
| Montalto et al. | 2021 | method | $d \lesssim 2.5 \text{ kpc}$ | |

Table 3. Extinction sources

* Distance from the Sun.

** Distance from the Sun in the Galactic disk.

notice that for lower metallicity ($[\frac{Fe}{H}] = -2.2$) the two sets of isochrones are in a good agreement in the turn-off point region, but BaSTI isochrones have slightly bluer in the main sequences and red giant branch is more vertical. Instead, for higher metallicity ($[\frac{Fe}{H}] = -1.2$) the shift between isochrones is more evident. BaSTI isochrones are fainter and redder. The reason for this shift could be that they take into account α -enhancement that displaces isochrones towards higher metallicity (Salaris et al. (1993)). Tab.2 gives a summary of the isochrones we used in this study.

In order to use Padova isochrones properly, we need to correct them for α -enhancement. To do so we used the technique proposed by Salaris et al. (1993) where α -enhanced isochrones can be reproduced by standard isochrones if a metallicity given by the following equation is used:

$$Z = Z_0(0.638f_\alpha + 0.362) \quad (1)$$

where $f_\alpha = \frac{Z}{Z_{Sun}} = 10^{[\frac{\text{element abundance}}{Fe}]}$

The result of α -correction is shown in Fig.2. In this plot we can see that the correction for α -enhancement increases the total metallicity on average by 0.2 dex. Moreover, Fig.6 indicates a good agreement between the stars' distribution and the isochrones, both colour-coded with metallicity.

4. REDDENING

In this work we used two photometric systems: Gaia (G , G_{BP} , G_{RP}) and Johnson (B, V). Both of them cover the optical part of the spectrum thus they are quite sensitive to reddening. Therefore, correction for reddening is a critical step in our analysis. Our targets are located in the Galactic Halo ($|b| > 20^\circ$). Galactic Halo is poor in gas and dust and, as a consequence, it does not exhibit significant extinction. But even small reddening corrections might cause big uncertainties in age determination, that is why we used the 5 different sources of extinction values listed in Tab.3 to get the best estimate for that effect.

Schlegel et al. (1998) is a full-sky 100 μm 2D map that is a reprocessed composite of the COBE/DIRBE and IRAS/ISSA maps, where the zodiacal foreground and confirmed point sources are removed. The uncertainty of the map is around 16%.

Schlafly & Finkbeiner (2011) presented a full-sky 2D dust reddening map measured as the difference between the measured and predicted colours of a star, as derived from stellar parameters from the Sloan Extension for Galactic Understanding and Exploration Stellar Parameter Pipeline. They achieve uncertainties of 56, 34, 25, and 29 mmag in the colors u - g, g - r, r - i, and i - z, per star, though the uncertainty varies depending on the stellar type and the magnitude of the star.

StarHorse extinction values are computed by Bayesian isochrone fitting technique with stellar parameters (T_{eff} , $\log g$, $[\frac{M}{H}]$) from spectroscopy, photometric magnitude (m_λ), parallax from Gaia DR2, and PARSEC isochrones. The extinction uncertainties are ~ 70 mmag, when all photometric information is available, and ~ 170 mmag if optical photometry is missing. For our data set the most common value of uncertainty is ~ 200 mmag. (See also Sec. 5.4) They provide an coverage of the disc close to the Galactic mid-plane ($|Z_{Gal}| < 1kpc$) from the Galactic center out to $R_{Gal} \sim 20kpc$.

Green et al. (2018) produced a new 3D map of interstellar dust reddening, covering three-quarters of the sky (declinations of $\delta \gtrsim -30^\circ$) out to a distance of several kiloparsecs. The map is based on high-quality stellar photometry of 800 million stars from Pan-STARRS 1 and 2MASS. They divide the sky into sightlines containing a few hundred stars each, and then infer stellar distances and types, along with the line-of-sight dust distribution. For our data set the mean uncertainty of this map is about 20 mmag.

Lallement et al. (2018) selected low-reddening SDSS/APOGEE-DR14 red giants to obtain an empirical effective temperature- and metallicity-dependent photometric calibration in the Gaia G and 2MASS Ks bands. This calibration has been combined with Gaia G-band empirical extinction coefficients recently published, G, J, and Ks photometry, and APOGEE atmospheric parameters to derive the extinction of a large fraction of the survey targets. Distances were estimated independently using isochrones and the magnitude-independent extinction K_{J-Ks} . This new data set has been merged with the one used for the earlier version of the dust map. A new Bayesian inversion of distance-extinction pairs has been performed to produce an updated 3D map that covers $4000 \times 4000 \times 600 pc^3$ around the Sun. Uncertainty of this map for our data set varies from 10 to 150 mmag.

To extent Lallement et al. (2018) map to farther distances we applied the method illustrated in Montalto et al. (2021). They suggested to use the dust distribution model of the Milky Way to calculate the amount of dust between the edge of the Lallement et al. (2018) map and the real position of the object. It can be applied if in there is no specific dust and gas structures which is almost true for the Halo where all stars under consideration are located. In Montalto et al. (2021) the extension method was applied for stars not farther than 2.5 kpc and tested to show good agreement with the photometric parameters.

To get the best extinction estimate for our stars we studied all sources of reddening corrections listed in Tab.3. Since the range in distances for our stars is from 0.2 to 30 kpc (see Sec. 5) it is more precise to use a 3D map instead of 2D, which additionally has lower accuracy. In Fig.3 we can see that Lallement et al. (2018) extended by Montalto et al. (2021) and Green et al. (2018) are in a good agreement with each other and with Schlegel et al. (1998) 2D map for far distances, for closer to the Sun star Schlegel et al. (1998) map reddening is greater. **StarHorse** reddening instead shows a larger dispersion in all distance range and on average larger reddening values compared to Schlegel et al. (1998) map. Therefore by comparing the three latest 3D maps we made a choice to use only Lallement et al. (2018) extended by Montalto et al. (2021) and Green et al. (2018). Both these maps have weak points. For example, Green et al. (2018) map covers only three-quarters of the sky. Lallement et al. (2018) does not have high accuracy in all directions. That is why our solution was to combine two reddening maps together by choosing for each star the best extinction estimate from Lallement et al. (2018) extended by Montalto et al. (2021) 3D map or from Green et al. (2018) 3D map. The resulting reddening correction is shown in Fig.4. We can see that the combined map shows the smallest stars' dispersion in the color-magnitude diagram (CMD).

5. DISTANCE DETERMINATION

Stellar distances constitute a fundamental quantity in astrophysics. In fact we need distances to compute absolute magnitudes for each metal-poor star in our data set. Distance is one of the crucial parameters that affect the obtained results. For this purpose we used four different techniques: Gaia DR3 parallaxes (Gaia Collaboration et al. (2022)), Gaia EDR3 (Gaia Collaboration (2021)) corrected by Lindegren et al. (2021), the distances derived by Bailer-Jones et al. (2021), and Queiroz et al. (2019) (**StarHorse**).

5.1. Gaia Data Release 3 (Gaia DR3) parallaxes

The first main technique is parallax distance. Today we have very accurate trigonometric parallaxes (see for uncertainties Tab.4) obtained by the Gaia satellite for about 1,47 billion stars (Gaia Collaboration et al. (2022)). From these trigonometric parallaxes, distance can be obtained through the following equation:

$$d = \frac{1}{\pi} \quad (2)$$

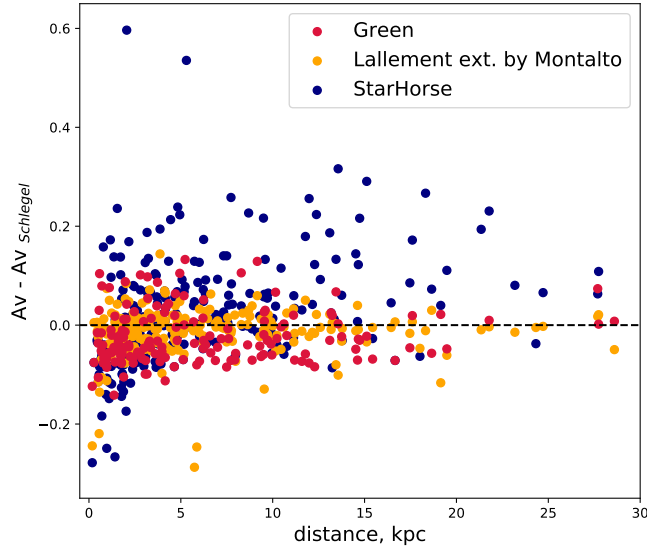


Figure 3. Comparison of reddening from Green et al. (2018), Lallement et al. (2018) extended by Montalto et al. (2021) and StarHorse with reddening from Schlegel et al. (1998) as a function of distance.

| Data product | Typical uncertainty | | | |
|---------------------------|---------------------|--------|--------|--------|
| | G < 15 | G = 17 | G = 20 | G = 21 |
| Five-parameter astrometry | | | | |
| position, mas | 0.01 - 0.02 | 0.05 | 0.4 | 1 |
| parallax, mas | 0.02 - 0.03 | 0.07 | 0.5 | 1.3 |
| Six-parameter astrometry | | | | |
| position, mas | 0.02 - 0.03 | 0.08 | 0.4 | 1 |
| parallax, mas | 0.02 - 0.04 | 0.1 | 0.5 | 1.4 |

Table 4. Uncertainties of Gaia Data Release 3 astrometry from Gaia Collaboration (2021)

where d is the distance to the object in pc and π is its trigonometric parallax in arcsecs. The problem with this distance determination is that, due to the structure of this equation, uncertainties on the distance are not symmetric around the mean value, especially for a large uncertainty on the parallax. That is why errors for each source must be computed separately for the higher and lower edges of the distance:

$$d_{low} = \frac{1}{\pi + \Delta\pi} \quad (3)$$

$$d_{high} = \frac{1}{\pi - \Delta\pi} \quad (4)$$

Uncertainties of Gaia Data Release 3 astrometry as given by the GAIA Collaboration are shown in Tab.4

5.2. Corrections for Gaia EDR3 parallaxes: Lindegren et al. (2021)

Parallaxes measured by Gaia Collaboration (2021) can have some biases that have been measured by Lindegren et al. (2021). Lindegren et al. (2021) found that parallaxes that correspond to quasars (distant objects, whose parallaxes should be distributed around zero) have a systematical offset from the expected distribution around zero, by a few tens of micro-arcsec. Based on quasars bias for faint sources they extended the map of the correction to lower magnitudes using physical pairs (binaries) and Large Magellanic Cloud sources. The parallax bias is found to depend in a non-trivial way on (at least) the magnitude, color, and ecliptic latitude of the source. Different dependencies apply to the five- and six-parameter solutions in Gaia EDR3. While it is not possible to derive a definitive recipe for the parallax correction, they give tentative expressions to be used at the researcher’s discretion and point out some possible paths

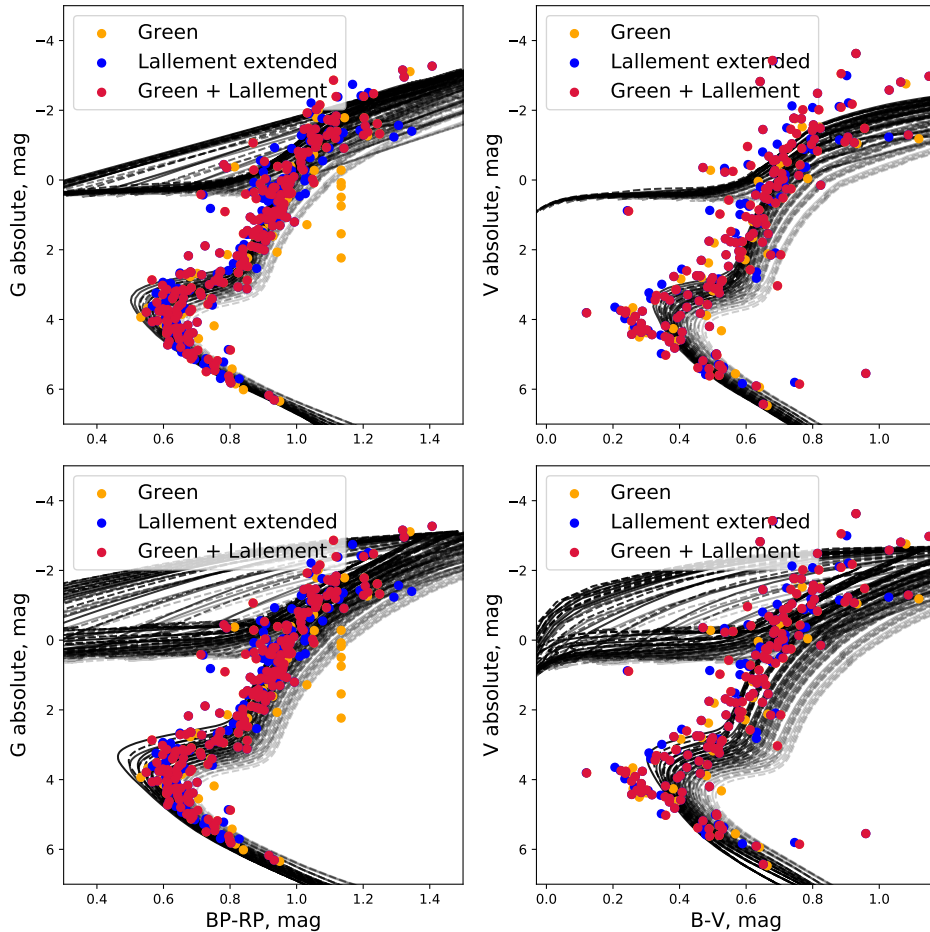


Figure 4. CMD in Gaia (1^{st} column) and Johnson (2^{nd} column) photometry corrected using Lallement et al. (2018) extended by Montalto et al. (2021), Green et al. (2018) and the best correction value from one of the two (Green+Lallement). 1^{st} row: Padova isochrones ([Fe/H]: -1.0 – -2.2 dex, age: 10 – 15 Gyr). 2^{nd} row: BaSTI isochrones ([Fe/H]: -1.0 – -3.2 dex, age: 10 – 15 Gyr).

toward future improvements. We applied the Lindegren et al. (2021) correction for downloaded Gaia EDR3 parallaxes and then computed distance and its lower and upper limit through Eq.(2), (4), (3). The results are shown in Fig.6 second row.

5.3. Corrections for Gaia EDR3 parallaxes: Bailer-Jones et al. (2021)

Despite Gaia EDR3’s high precision, the majority of stars observed by Gaia are distant or faint so their parallax uncertainties are large and this prevents the direct inversion of parallax for obtaining distance. That is why Bailer-Jones et al. (2021) used a probabilistic approach to estimate stellar distances that use a prior construction from a three-dimensional model of our Galaxy. This model includes interstellar extinction and Gaia’s variable magnitude limit. They obtain two types of distances. The first, geometric, uses the parallax together with a direction-dependent prior on distance. The second, photo-geometric, additionally uses the color and apparent magnitude of a star, by exploiting the fact that stars of a given color have a restricted range of probable absolute magnitudes (plus extinction). Tests on simulated data and external validations show that the photo-geometric estimates generally have higher accuracy and precision for stars with poor parallaxes.

5.4. StarHorse distances

An additional source of distances is the APOGEE DR16 StarHorse catalog where Queiroz et al. (2019) combined spectroscopic (APOGEE-2 survey Data Release 16) and photometric (IR: 2MASS, AllWISE; Optical: PanSTARRS-1)

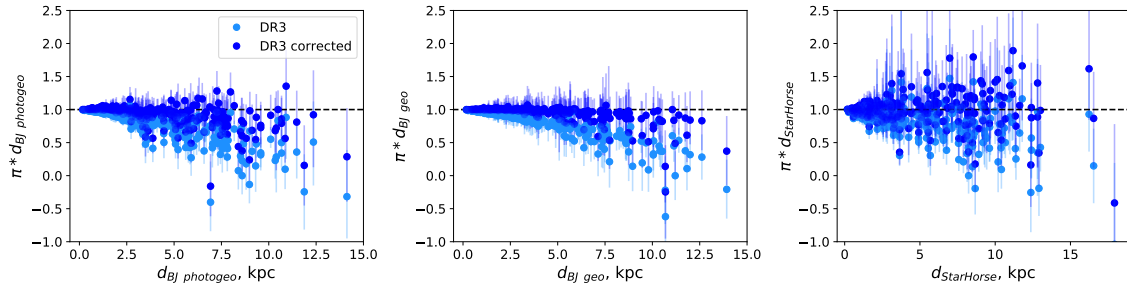


Figure 5. Comparison of parallax from Gaia DR3 (light blue) and corrected Gaia EDR3 by Lindegren et al. (2021) (blue) with geometric (*left*) and photogeometric (*middle*) distance from Bailer-Jones et al. (2021) and with StarHorse distance from Queiroz et al. (2019) (*right*). The vertical axis shows the Gaia DR3 parallax and corrected parallax multiplied by the geometric distance: values under 1 correspond to the parallax distance being larger than the value of Bailer-Jones et al. (2021)/StarHorse distance and vice versa. The vertical error bars take into account the statistical uncertainties both on the parallax and the distance, but the horizontal error bars for the distance are not displayed.

data as well as parallaxes (Gaia Data Release 2). They used Bayesian isochrone-fitting code StarHorse to obtain distances and extinction for 388 815 APOGEE stars. All studied in this work stars are included. The typical distance uncertainties are $\sim 6\%$ for APOGEE giants and $\sim 2\%$ for APOGEE dwarfs. StarHorse uncertainties vary with the input spectroscopic catalogue, available photometry, and parallax uncertainties. Data are available at <https://data.aip.de/projects/aqueiroz2020.html>.

5.5. Distance choice

The comparison of distances from Bailer-Jones et al. (2021) and parallaxes from Gaia DR3 and corrected by Lindegren et al. (2021) are shown in Fig.5 (left, middle panels). The vertical axis shows the Gaia DR3 parallax and corrected parallax multiplied by the geometric (Fig.5, left panel) and photo-geometric (Fig.5, middle panel) distance: values under 1 correspond to the parallax distance larger than the value of Bailer-Jones et al. (2021) distance and vice versa. The vertical error bars take into account the statistical uncertainties both on the parallax and on the distance, but the horizontal error bars for the distance are not displayed. We can see that for close objects (< 3 kpc) parallaxes corrected by Lindegren et al. (2021) are in good agreement with Bailer-Jones et al. (2021) geometric and photo-geometric distances. Beyond 3 kpc the corrected parallaxes give larger distances than the geometric and the photo-geometric ones. In general Gaia DR3 parallaxes yield larger distances in all ranges of distances. Some of the stars have negative parallaxes but positive distances can be derived from Bailer-Jones et al. (2021).

From Fig.5 (right panel) we can notice that StarHorse distances and distances from parallax corrected by Lindegren et al. (2021) are in a good agreement. On the contrary, direct distances from Gaia EDR3 parallaxes show larger values. However, to consider the best estimate of distances for our data set a deeper investigations should be done using a CMD and isochrone fitting technique. In Fig.6 stars are corrected for reddening with combined Green et al. (2018) + Lallement et al. (2018) extended by Montalto et al. (2021) map and color-coded with corrected metallicity for Padova isochrones, observed - for BaSTI isochrones. Metallicity range for Padova isochrones: $-1.3 - -2.2$ dex, for BaSTI isochrones: $-1.3 - -3.2$ dex. For each metallicity 10 and 15 Gyr isochrone are plotted colour-coded with metallicity. Comparing different methods for distance determination we can highlight the following discrepancies, depending on the distance technique we use:

- Some stars are located in low probability regions, like above the MS and below the SGB, or on the red side of the RGB. (Gaia DR3 parallaxes, Lindegren, Bailer-Jones, StarHorse)
- Non negligible shift in the position of RGB and TO stars in comparison with the isochrones of the same metallicity. (Lindegren, Bailer-Jones, StarHorse)
- Different shape of the targets RGB if compared with the shape of isochrone RGB. (Lindegren, Bailer-Jones, StarHorse)

According to the listed above criteria, we can conclude that Gaia parallaxes show the best fit to the data. In this case we can see also that fewer targets only are lying in the low probability region. Moreover, all stars with

| | B | V | I | G | G_{BP} | G_{RP} |
|-----------------|-------|-------|-------|-------|----------|----------|
| A_λ/A_V | 1.326 | 1.000 | 0.599 | 0.861 | 1.061 | 0.648 |

Table 5. Reddening coefficients for different photometric filters

metallicities lower than the lower limit for isochrones metallicity range lie above RGB where the estimated position of these stars should be. Lindegren correction and **StarHorse** distances move low metallicity stars in RGB to the position of isochrones with higher metallicity and break the shape of RGB. Bailer-Jones additionally shift more stars to the low probability region which reduces the quality of the data set. All these tests show that the best distance estimate estimator for our purposes is the distance obtained directly inverting Gaia parallaxes.

A possible explanation for the lower accuracy we obtained applying Lindegren et al. (2021) correction is that they are based on faint sources and, as a consequence, they are less accurate for brighter magnitudes as it is the case for our targets. Bailer-Jones also used Lindegren correction as an input. Because of this, their corrections are affected by the same bias. **StarHorse** distances are less precise instead because Queiroz et al. (2019) used Gaia Data Release 2 parallaxes as prior for the distance calculation, which have lower accuracy compared with new Gaia DR3 parallaxes.

6. DERIVATION OF THE ABSOLUTE MAGNITUDE

To be able to compare isochrones with observational data we need to convert observed G photometry to its absolute magnitude. To do this we need to apply distance modulus and reddening correction using:

$$M_\lambda = m_\lambda + 5 - 5 \cdot \log(d) - A_\lambda$$

where d is the distance to the star in parsecs and $A_G = A_V \cdot coef$ (for *coef* see Tab.5). These transformations assume the standard reddening law $A_V = R_V \cdot E(B - V)$ with $R_V = 3.1$ since all our targets are far from the galactic plane or the galactic Bulge, where R_V can assume different values.

7. DIFFERENCE IN CMDS FOR DIFFERENT PHOTOMETRIC SYSTEMS

A closer look at the data evidences additional peculiarities. Fig.6 shows that part of TO stars in the Johnson photometry (the two columns on the right) are blue-shifted with respect to the isochrones and also if compared with their position in the Gaia photometry (the two columns on the left). In order to investigate deeper this behaviour we performed further tests.

First of all, we colour-coded our data with Galactic latitude (Fig.7, top row). The bottom left panel of this figure report the position of the targets on the V vs. B-V CMD. It is clear that all the stars with the larger TO-shift are located at positive Galactic latitude, while all the other stars have negative Galactic latitudes. The difference in position might indicate a difference in reddening, but since our data set is corrected for it, only a particularly improbable kind of extinction could explain this behaviour. On the other hand Fig.7 (bottom right panel) reports the V vs. V-I CMD, where we do not see such an affect. This means that the shift is entirely due to the B filter.

7.0.1. Chemical analysis

One of the reasons why stars with the same temperature (as inferred from the BP-GP and V-I colors) and luminosity (as inferred from G and V magnitudes) differ in just one of the filters, is that this filter contains strong molecular bands and that the elements responsible for these band (usually C,N,O) vary their abundances from one star the other. Also chemical abundances variation of C, N, O, Ne, Mg, Si, S, Ca, Fe affect opacity of the star and change the continuum emission in that part of the spectrum (Salaris et al. (1993)). To check these effects we download from the ESO database⁵ flux-calibrated UVES spectra for couples of stars with the same T_{eff} and similar reddening ($\Delta A_V < 0.02$ mag) but different dereddened B-V colors. In Fig.8 we can see that when the distance between shifted (yellow) and non-shifted (blue) stars increases, also the continuum of the shifted stars increases. It happens specifically in the range of the B filter. To check the dependence between the shift and chemical composition, we colour-coded CMDs with abundances of C (the only element responsible of molecular bands we have) and Fe. From Fig.9 we can see that shifted stars are enhanced in C and more metal-poor on average. Since we see no presence of strong molecular bands in the spectra, we conclude it is the change in the opacity of the atmospheres of the stars due to the different

⁵ <http://archive.eso.org/vs/scienceportal/home>

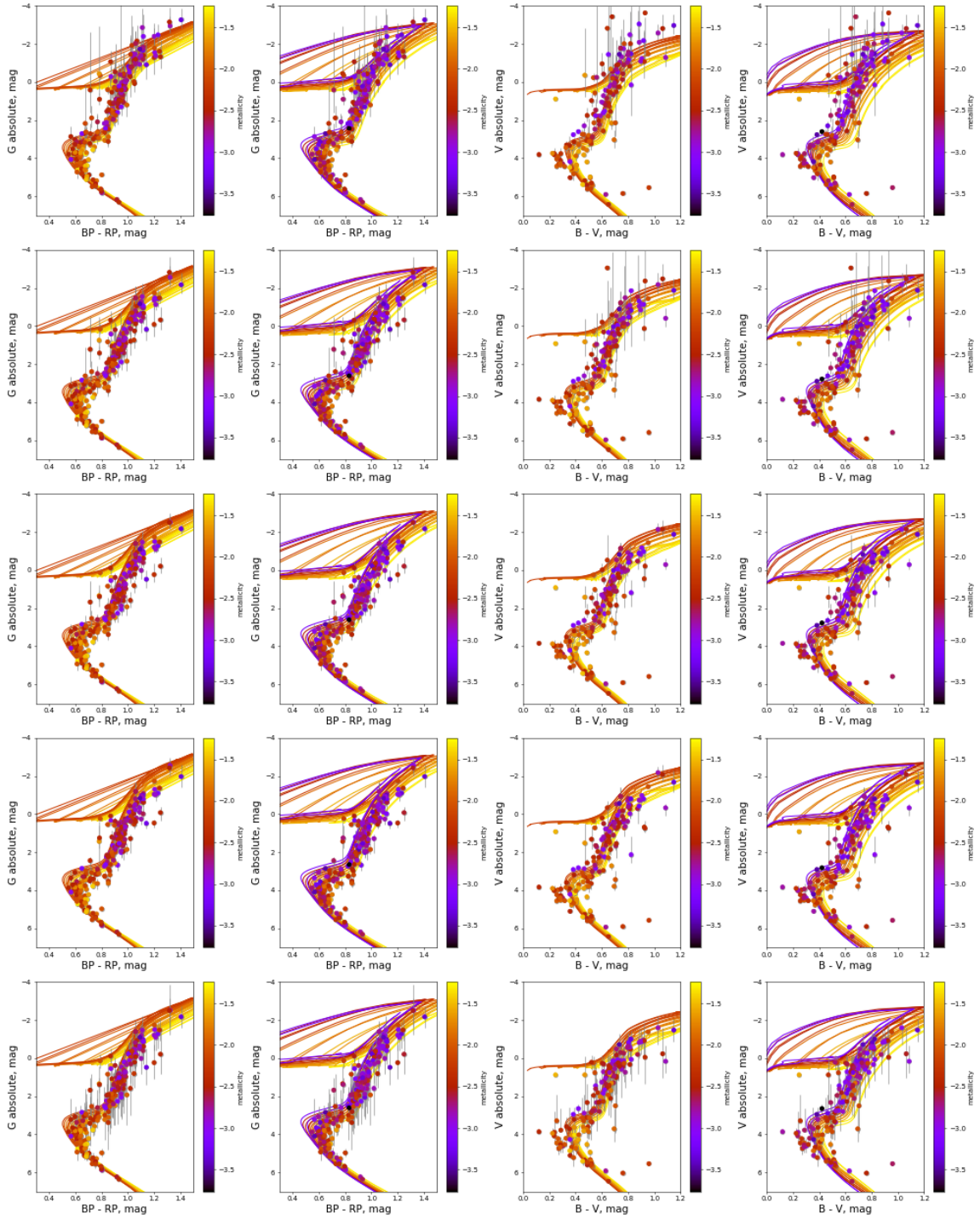


Figure 6. Gaia (*first two columns*) and Johnson (*last two columns*) photometry color-coded with corrected metallicity for Padova isochrones (*1st, 3rd columns*) and with observed metallicity for BaSTI isochrones (*2nd, 4th columns*). Distances are computed by Gaia DR3 parallaxes (*1st row*), Gaia EDR3 parallaxes corrected by Lindegren et al. (2021) (*2nd row*), Bailer-Jones et al. (2021) (geo: *3rd row*, photgeo: *4th row*), and computed by Queiroz et al. (2019) (StarHorse) (*5th row*). Isochrones are colour-coded with metallicity ([Fe/H]: -1.0 – -2.2 dex, age: 10 – 15 Gyr (Padova); [Fe/H]: -1.0 – -3.2 dex, age: 10 – 15 Gyr (BaSTI))

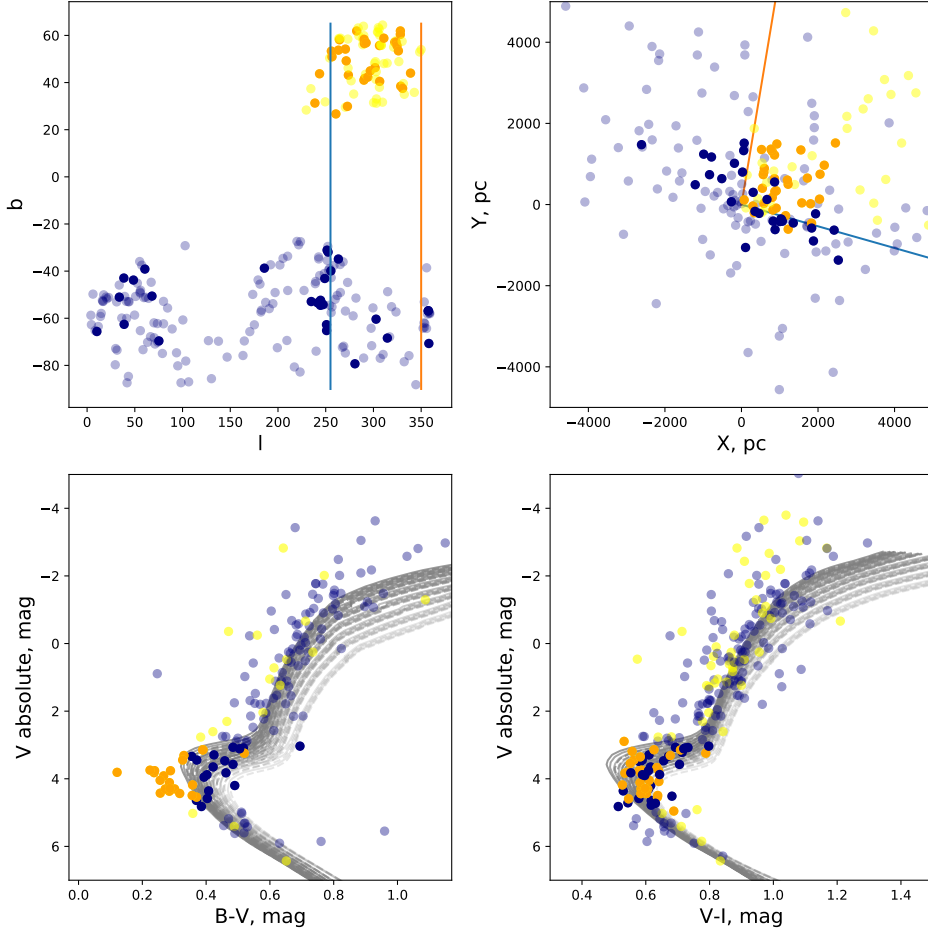


Figure 7. *Top:* Position of our targets on the sky (*left*, Galactic coordinates) and in the Galactic plane (*right*), color-coded with Galactic latitude ($b > 0$: yellow, $b < 0$: blue). *Bottom:* CMD in V vs. B-V (*left*) and V vs. V-I (*right*) filters, yellow points are non-TO stars with $b > 0$, orange points are TO stars with $b > 0$, light blue are non-TO stars with $b < 0$, while dark blue are TO stars with $b < 0$. Padova isochrones are added as a reference ([Fe/H]: -1.0 – -2.2 dex, age: 10 – 15 Gyr).

C and Fe contents that is the cause of shift in the B-V color. Specifically higher [C/Fe] abundance and lower [Fe/H] content increase the flux in the B filter.

For this reason Johnson photometry can not be properly used for age determination for very metal-poor stars. Gaia filters are wider and so less affected by this phenomenon and it is the only photometry we will use for the age determination.

8. AGE DETERMINATION METHOD

To derive age we developed an automatic technique based on isochrone fitting. First, we filtered our data with the following criteria:

1. Distance > 0
2. Distance error $< 20\%$
3. Metallicity range: -2.3 – -1 dex for Padova isochrone; -3.3 – -1 dex for BaSTI isochrone
4. Absolute magnitude is in TO-point region: $2.4 < G < 4.7$ mag

The first two criteria exclude stars with bad astrometric measurements. The third cutoff is based on the metallicity range covered by isochrone data sets. We should note that for different isochrones the cutoff is different. And the

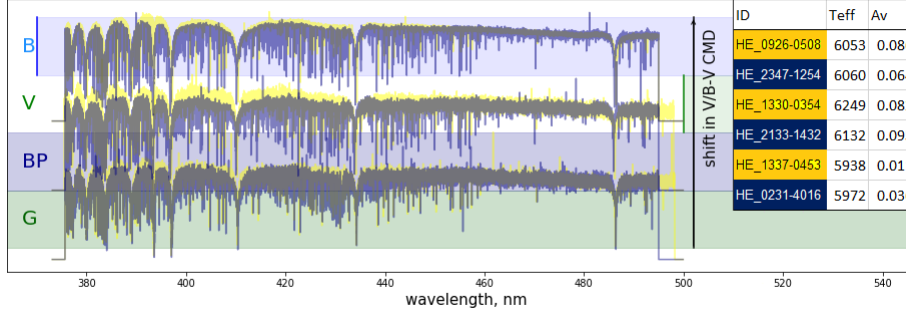


Figure 8. Comparison of the spectra for bluer and redder stars in V/B_V CMD. Gaia and Johnson photometric filters ranges are plotted with color.

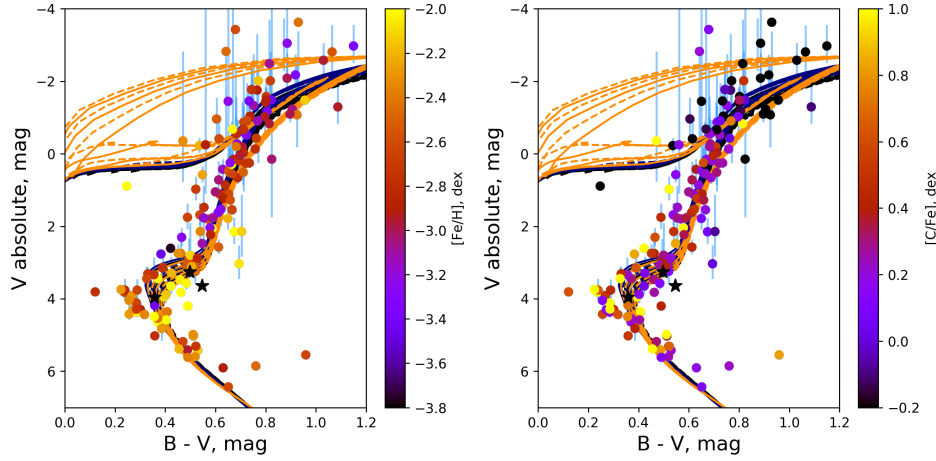


Figure 9. Johnson photometry color-coded with $[\text{Fe}/\text{H}]$ (left panel) and $[\text{C}/\text{Fe}]$ (right panel). Distance computed by means of Gaia DR3 parallaxes. Black stars are stars: HD 84937, HD 132475, and HD 140283 (VandenBerg et al. (2014)). Padova (blue) and BaSTI (orange) isochrones with $[\text{Fe}/\text{H}] = -2.2$ dex, age: 10 – 15 Gyr are added as a reference.

fourth cutoff leaves only stars from the TO-point region - the part of the CMD most sensitive to age. The algorithm takes a set of isochrones matching the metallicity of the target and searches for the closest. Each isochrone is defined by a set of X,Y points in the 2D space of the CMD. The distance used to choose the closest isochrone is the shortest between the perpendicular to one of the segments defined by two consecutive X,Y points, and the distance to the closest point of the isochrone. The age of the closest isochrone is then considered as a first guess of age of the star if the distance is less than 10^{-4} mag (the maximum distance between isochrones with age step 100 Myr). Otherwise, age can not be derived, since the star is too far from all isochrones.

As a second step, we consider the mean parallax, reddening, metallicity, and photometry of each target and the related errors. Assuming a gaussian distribution we randomly distributed 10.000 points in the parameter space and applied the age determination technique to each of them. The result is an age histogram that is fitted with a Gaussian function. We consider its mean as the age of the star and σ as its uncertainty.

In Fig.10 we can see an illustration of the age determination for Padova and BaSTI isochrones. Isochrones have an upper limit of 20 Gyr for Padova, and from 15.4 to 19.2 Gyr (depending on metallicities) for BaSTI. Because of this, all stars redder than the oldest isochrone are considered to have the age of this isochrone. Therefore, we get some saturation in the bin corresponding to the oldest isochrone. We cut saturated bins as not representative. We derived age in three different combinations of photometric filters: G vs. $G_{BP}-G_{RP}$, G vs. $G_{BP}-G$, G vs. $G-G_{RP}$.

To get the best age sample we applied the following criteria:

1. Age derived in all three filter combinations: G vs. $G_{BP}-G_{RP}$, G vs. $G_{BP}-G$, G vs. $G-G_{RP}$.

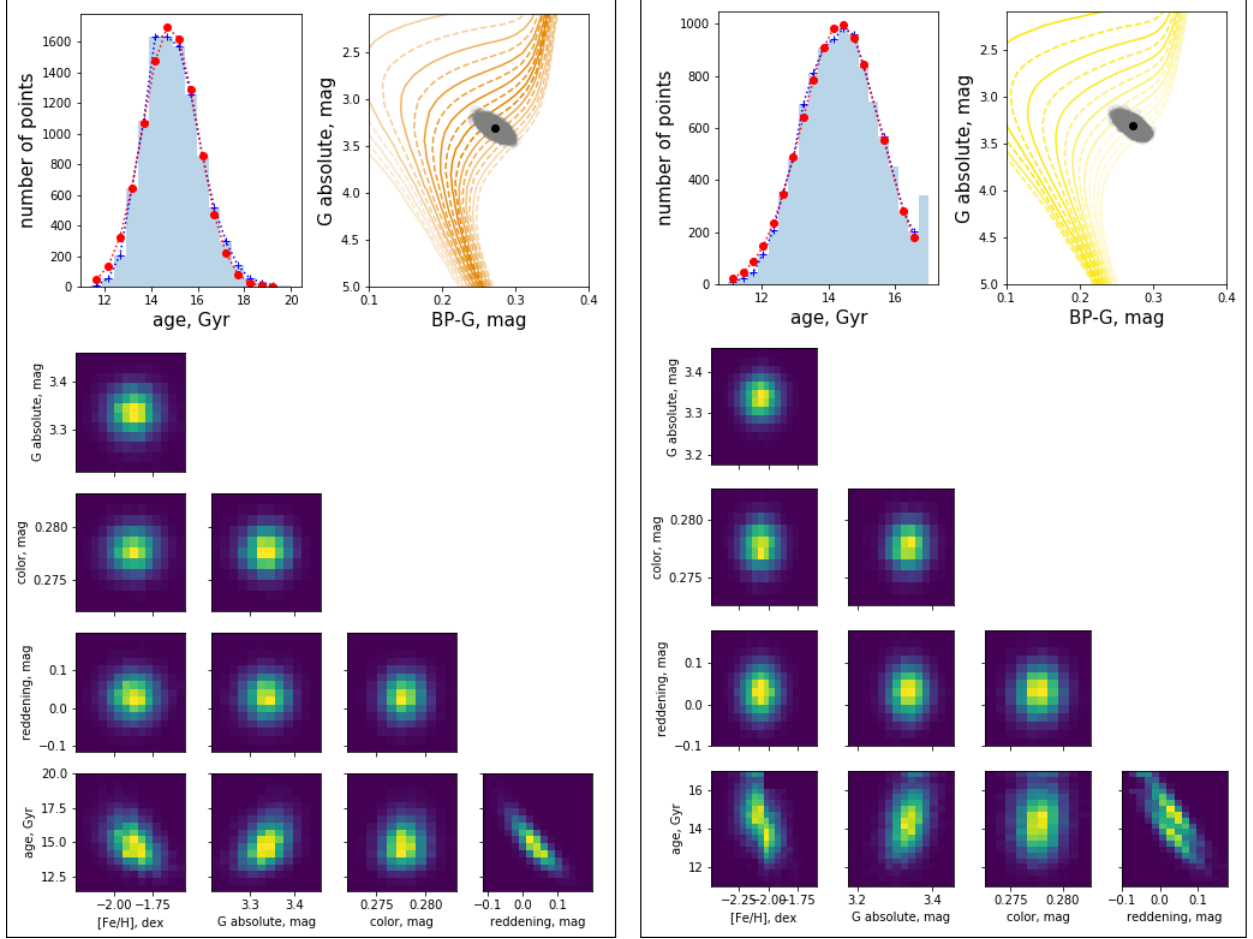


Figure 10. Resulting plot of age determination from Padova (*left panel*) and BaSTI (*right panel*) isochrones for star HE 0023–4825 in diagrams G vs. BP-G. Grey dots in the CMD are randomly selected input parameters. Black dot is original stellar parameters.

2. Derived age is not closer to the oldest isochrone less than 1σ .

In this way we reduced the targets for which we can derive good ages to 28.

Table 6. Age of metal-poor stars.

| ID | [$\frac{Fe}{H}$] | age from Padova isochrones, Gyr | | | age from BaSTI isochrones, Gyr | | | average, Gyr | | | | | |
|--------------|--------------------|---------------------------------|-------------|-------------|--------------------------------|-------------|-------------|--------------|-----------|--------------|-----------|------|------|
| | | G vs. G-GRP | G vs. G-GRP | G vs. G-GRP | G vs. G-GRP | G vs. G-GRP | G vs. G-GRP | G vs. G-GRP | BaSTI | Padova+BaSTI | | | |
| dex | | age | error | age | error | age | error | age | error | age | error | | |
| HE 0023-4825 | -2.06 | 14.8 | ± 1.2 | 14.9 | ± 1.1 | 14.4 | ± 1.2 | 14.4 | ± 1.2 | 14.9 | ± 1.2 | 14.4 | 14.6 |
| HE 0109-3711 | -1.91 | 11.8 | ± 2.3 | 11.9 | ± 2.4 | 11.6 | ± 2.7 | 11.8 | ± 2.7 | 11.8 | ± 2.7 | 11.7 | 11.8 |
| HE 0231-4016 | -2.08 | 13.3 | ± 1.3 | 13.3 | ± 1.2 | 15.4 | ± 1.3 | 15.4 | ± 1.2 | 13.3 | ± 1.2 | 15.4 | 14.4 |
| HE 0340-3430 | -1.95 | 13.6 | ± 0.9 | 13.6 | ± 0.9 | 12.9 | ± 0.9 | 13.1 | ± 0.9 | 13.6 | ± 0.9 | 13.0 | 13.3 |
| HE 0430-4404 | -2.07 | 7.7 | ± 3.0 | 6.6 | ± 2.7 | 7.0 | ± 2.8 | 13.8 | ± 2.8 | 7.1 | ± 2.6 | 13.2 | 10.1 |
| HE 0447-4858 | -1.69 | 14.0 | ± 2.1 | 13.4 | ± 1.7 | 13.1 | ± 2.1 | 12.7 | ± 1.9 | 13.7 | ± 2.0 | 12.9 | 13.3 |
| HE 0501-5139 | -2.38 | 9.0 | ± 2.3 | 9.0 | ± 2.3 | 8.9 | ± 2.4 | 8.9 | ± 2.4 | 9.0 | ± 2.4 | 8.9 | 8.9 |
| HE 0519-5525 | -2.52 | 13.3 | ± 1.8 | 13.6 | ± 1.8 | 13.3 | ± 1.6 | 13.6 | ± 1.6 | 13.5 | ± 1.6 | 13.4 | 13.5 |
| HE 0534-4615 | -2.01 | 16.0 | ± 2.9 | 16.0 | ± 2.9 | 13.8 | ± 2.3 | 13.8 | ± 2.2 | 16.0 | ± 2.2 | 13.8 | 14.9 |
| HE 0938+0114 | -2.51 | 12.4 | ± 1.9 | 13.8 | ± 1.8 | 13.8 | ± 1.7 | 14.6 | ± 1.0 | 13.1 | ± 1.2 | 14.2 | 13.7 |
| HE 1052-2548 | -2.29 | 15.3 | ± 0.7 | 16.1 | ± 0.6 | 15.2 | ± 0.5 | 16.0 | ± 0.4 | 15.7 | ± 0.4 | 15.7 | 15.7 |
| HE 1105+0027 | -2.42 | 11.2 | ± 2.1 | 11.4 | ± 2.2 | 12.8 | ± 2.4 | 12.9 | ± 2.4 | 11.3 | ± 2.4 | 12.8 | 12.1 |
| HE 1225-0515 | -1.96 | 14.6 | ± 1.6 | 14.6 | ± 1.6 | 14.7 | ± 1.8 | 14.6 | ± 1.6 | 14.6 | ± 1.8 | 14.7 | 14.6 |
| HE 1330-0354 | -2.29 | 12.3 | ± 0.9 | 13.3 | ± 0.8 | 13.7 | ± 0.9 | 14.6 | ± 0.8 | 12.8 | ± 0.8 | 14.2 | 13.5 |
| HE 2250-2132 | -2.22 | 13.2 | ± 1.2 | 13.6 | ± 1.3 | 12.8 | ± 1.1 | 13.2 | ± 1.3 | 13.4 | ± 1.2 | 13.0 | 13.2 |
| HE 2347-1254 | -1.83 | 14.6 | ± 1.7 | 14.6 | ± 1.5 | 14.5 | ± 1.6 | 14.6 | ± 1.4 | 14.6 | ± 1.4 | 14.5 | 14.6 |
| HE 2347-1448 | -2.31 | 8.7 | ± 1.8 | 8.8 | ± 1.8 | 8.4 | ± 1.8 | 8.5 | ± 1.9 | 8.8 | ± 1.9 | 8.5 | 8.6 |
| HE 0244-4111 | -2.56 | ... | ... | ... | ... | 12.6 | ± 1.3 | 13.0 | ± 1.3 | ... | ± 1.3 | 12.7 | ... |
| HE 0441-4343 | -2.52 | ... | ... | ... | ... | 10.3 | ± 1.9 | 10.5 | ± 1.9 | ... | ± 1.9 | 10.4 | ... |
| HE 0513-4557 | -2.79 | ... | ... | ... | ... | 12.5 | ± 2.5 | 12.4 | ± 2.5 | ... | ± 2.5 | 12.4 | ... |
| HE 0926-0508 | -2.78 | ... | ... | ... | ... | 14.6 | ± 0.8 | 14.9 | ± 0.6 | ... | ± 0.7 | 14.8 | ... |
| HE 1006-2218 | -2.69 | ... | ... | ... | ... | 12.7 | ± 1.1 | 13.1 | ± 0.8 | ... | ± 0.9 | 12.9 | ... |
| HE 1015-0027 | -2.66 | ... | ... | ... | ... | 14.9 | ± 1.3 | 15.6 | ± 1.0 | ... | ± 1.0 | 15.2 | ... |
| HE 1120-0153 | -2.77 | ... | ... | ... | ... | 10.7 | ± 0.7 | 11.0 | ± 0.6 | ... | ± 0.6 | 10.8 | ... |
| HE 1126-1735 | -2.69 | ... | ... | ... | ... | 9.4 | ± 2.6 | 9.5 | ± 2.6 | ... | ± 2.6 | 9.4 | ... |
| HE 1413-1954 | -3.22 | ... | ... | ... | ... | 13.1 | ± 0.9 | 15.3 | ± 1.5 | ... | ± 1.2 | 14.2 | ... |
| HE 2222-4156 | -2.73 | ... | ... | ... | ... | 13.3 | ± 2.4 | 13.7 | ± 2.4 | ... | ± 2.4 | 13.5 | ... |
| HE 2325-0755 | -2.85 | ... | ... | ... | ... | 13.3 | ± 1.2 | 13.6 | ± 1.2 | ... | ± 1.2 | 13.6 | ... |

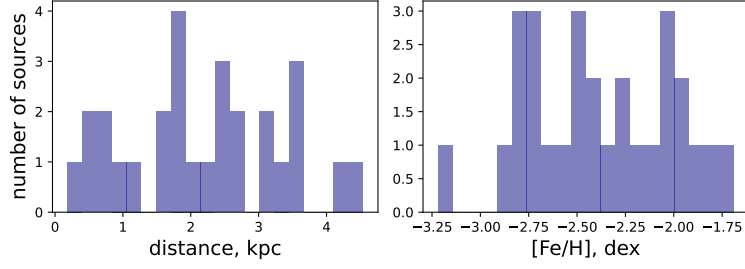


Figure 11. Distribution of the distance and metallicity for the 28 stars with derived age.

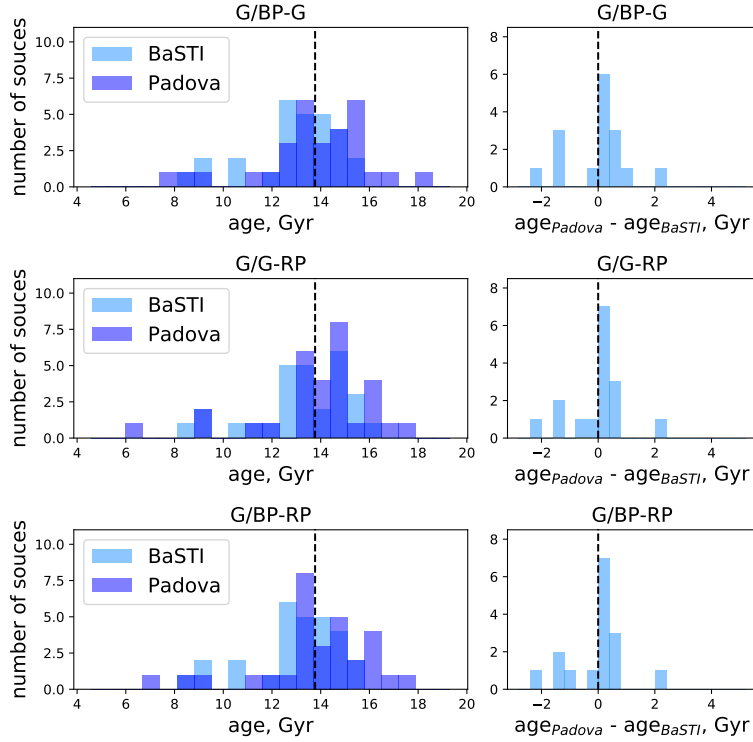


Figure 12. *Left:* dispersion in age determination from Padova and BaSTI isochrones in diagrams G vs. G_{BP-G} , G vs. G_{G-RP} , G vs. $G_{BP-G_{RP}}$. Vertical dotted line is the age of the Universe 13.77 Gyr (Bennett et al. (2013)). *Right:* dispersion in age difference between Padova and BaSTI isochrones in diagrams G vs. G_{BP-G} , G vs. $G_{G_{RP}}$, G vs. $G_{BP-G_{RP}}$. Vertical dotted line is a zero point.

9. RESULTS

9.1. Age

The derived ages for 28 selected stars are reported in Tab.6. The distribution of the distance and metallicity is reported in the Fig.11. Out of 28 we have only 17 stars for which age is derived from both isochrone sets and for 11 stars age was derived only from BaSTI isochrone set due to its lower limit in metallicity. In Fig.12 on the left we can see the dispersion of the age, where the vertical dotted line shows the age of the Universe 13.77 Gyr (Bennett et al. (2013)). On the right of Fig.12 shows that on average Padova isochrones show older age but the systematic difference is much less than 1 Gyr.

We also compared ages derived with different filter combinations: G vs. G_{BP-G} , G vs. $G_{G_{RP}}$, G vs. $G_{BP-G_{RP}}$. The result is reported in Fig.13 where we can notice that the peak of all distributions is compatible with zero within the errors. This means that ages derived with different filter combinations are the same.

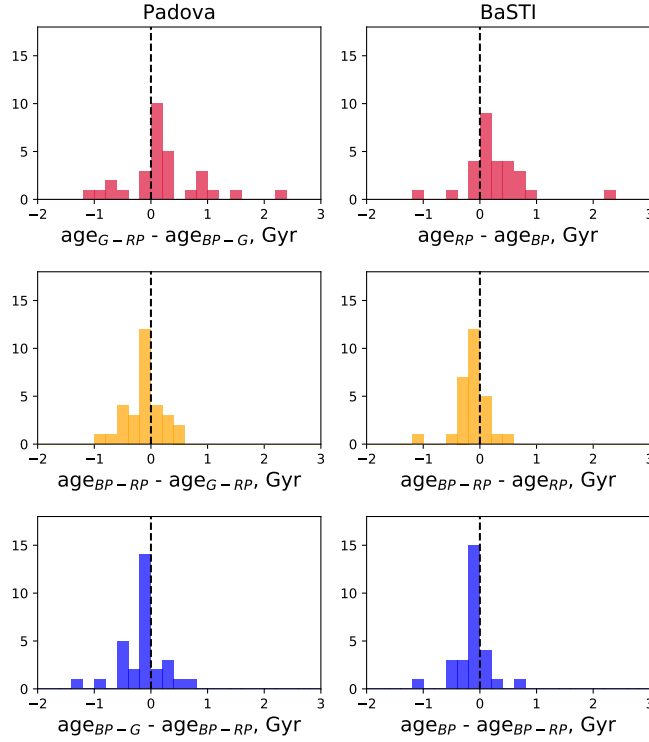


Figure 13. Dispersion of difference in age from different filter combinations: G vs. G_{BP-G} , G vs. $G-GRP$, G vs. G_{BP-GRP} for Padova and BaSTI isochrones. Vertical dotted line is zero-line.

| Name | [Fe/H] dex | age Gyr | π mas | d pc | A_v mag | age(ref.) Gyr |
|----------|---------------|------------|--------------|---------|--------------|------------------|
| NGC 6397 | -1.99 | 12.9 | 0.397 | 2519 | 0.614 | 12.6 |
| M 30 | -2.3 | 12.1 | 0.117 | 8547 | 0.170 | 13.0 |
| M 92 | -2.3 | 12.6 | 0.108 | 9259 | 0.072 | 12.5 |

Table 7. Globular cluster parameters

9.2. Comparison with old metal-poor globular clusters: M30, M92, and NGC 6397

We used metal-poor globular clusters (GCs) as a test of our age determination technique. We calculated the age for each star of GC located in the TO-point region ($2.4 < G < 4.7$ mag). All parameters for age determination of GC are listed in Tab.7. Parallax was derived as a mean parallax from Gaia DR3 of all members of the cluster. All three GC are located far from the Sun ($> 2.5kpc$). They lie outside the [Green et al. \(2018\)](#) reddening map, and far from the edge of the [Lallement et al. \(2018\)](#) reddening map that is why we choose extinction coefficients from 2D [Schlegel et al. \(1998\)](#) map. Metallicities are taken as an average of results listed in the SIMBAD catalog⁶. Reference ages were collected from [Correnti et al. \(2018\)](#) (NGC 6397), [Kains et al. \(2013\)](#) (M 30), [VandenBerg et al. \(2016\)](#) (M 92).

Firstly, we checked the accuracy of our automatic age determination method by comparing the age derived by different authors with our results. As we can notice in the Fig.14 that the age determined by our method is in a good agreement with ages derived by other authors. Only for M 30 age is slightly younger. This inconsistency is caused by uncertainties of input data, especially in parallax and reddening.

Secondly, we compare the distribution of the age of the GC with the age distribution of metal-poor stars. In Fig.14 we can see that on average our metal-poor stars are older than all three GCs by about 1 Gyr. Also, it is worth

⁶ <http://simbad.u-strasbg.fr/simbad/sim-fbasic>

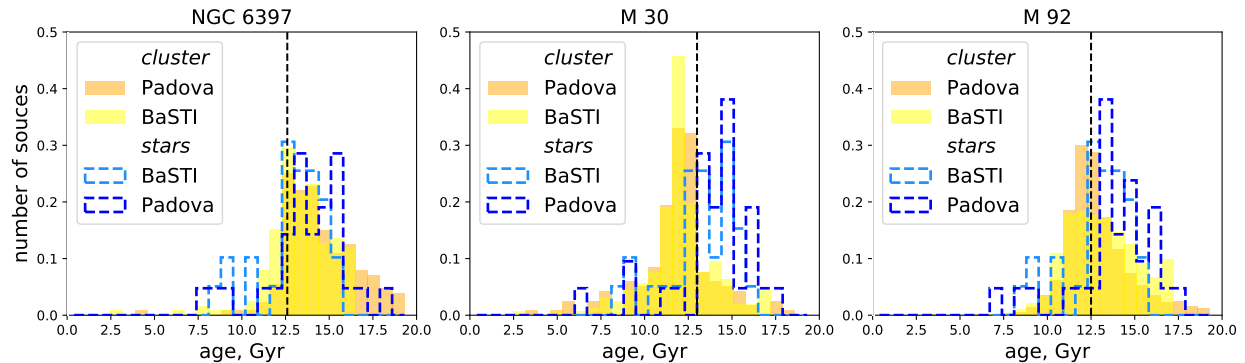


Figure 14. Dispersion of the age for GC NGC 6397, M 30, M92 compared with metal-poor stars under investigation.

| parameter | HD 84937 | HD 132475 | HD 140283 |
|---------------------|----------|-----------|-----------|
| G , mag | 8.207 | 8.391 | 7.036 |
| G_{BP} , mag | 8.423 | 8.692 | 7.321 |
| G_{RP} , mag | 7.817 | 7.898 | 6.562 |
| π , mas | 13.498 | 10.671 | 16.267 |
| $\Delta\pi$, mas | 0.044 | 0.025 | 0.026 |
| $[Fe/H]$, dex | -2.0 | -1.4 | -2.4 |
| $[\alpha/Fe]$, dex | 0.38 | 0.45 | 0.26 |
| A_V , mag | 0.009 | 0.047 | 0.006 |
| ΔA_V , mag | 0.047 | 0.056 | 0.053 |

Table 8. [VandenBerg et al. \(2014\)](#) star parameters

mentioning that the width of the GC’s age distribution shows that stars whose age is older than the age of the universe can be explained within the natural dispersion of the parameters in the same way as in GC.

9.3. Comparison with the three ancient stars HD 84937, HD 132475, and HD 140283

We made an additional sanity check by comparing our results with the three very old stars HD 84937, HD 132475, and HD 140283. They were studied by [VandenBerg et al. \(2014\)](#). HD 140283 was studied also by [Bond et al. \(2013\)](#). Both studies discovered that these stars are old and close to the age of the Universe. We used our age determination technique to derive their age. We used photometry and parallaxes from Gaia DR3, metallicity from the SIMBAD catalog⁷, and reddening from [Lallement et al. \(2018\)](#). All parameters are listed in Tab.8. The resulting ages are shown in the Tab.9. We can see that our results are close to the previously derived ages and they coincide within the uncertainties.

9.4. Age averaging

Finally, we calculated the arithmetic and weighted average age for all the stars (Tab.10). The average age is very close to the age of the Universe that means that most of the stars under consideration were born recently after the Big Bang. The provided uncertainties take into account only the formal internal errors. But obviously we may have additional error’s sources coming, for example, from isochrone’s models: convection treatment, element diffusion (settlement of heavy elements and consequent wrong global metallicity derived from the actual stellar atmosphere [Bonfanti et al. \(2015\)](#)) and temperature-color transformations. There are also subtle effects due to overabundance of oxygen on the ”shape” of the TO-point ([VandenBerg et al. \(2014\)](#)) and impact in opacity from C, Ca, Mg (Sec. 7.0.1). Another important external error could be the gas/dust ratio implied in the reddening derivation of the [Lallement et al. \(2018\)](#) map based on gas. We may reasonably suppose that they account for about 0.5 Gyr (this corresponds to an A_V error

⁷ <http://simbad.u-strasbg.fr/simbad/sim-basic>

| star | source | BaSTI | | Padova | |
|-----------|------------------------------------------|-------|------------|--------|------------|
| | | age | error | age | error |
| HD 84937 | G vs. G_{BP-G} | 13.18 | ± 1.40 | 12.03 | ± 1.41 |
| | G vs. $G-G_{RP}$ | 14.8 | ± 1.05 | 13.96 | ± 1.31 |
| | G vs. $G_{BP-G_{RP}}$ | 14.21 | ± 1.28 | 13.1 | ± 1.22 |
| | average | 14.06 | ± 1.51 | 13.03 | ± 1.79 |
| | VandenBerg et al. (2014) | 12.08 | ± 0.14 | | |
| HD 132475 | G vs. G_{BP-G} | 13.28 | ± 1.27 | 13.16 | ± 1.14 |
| | G vs. $G-G_{RP}$ | 14.16 | ± 1.27 | 14.09 | ± 1.32 |
| | G vs. $G_{BP-G_{RP}}$ | 13.68 | ± 1.14 | 13.64 | ± 1.18 |
| | average | 13.71 | ± 0.81 | 13.63 | ± 0.86 |
| | VandenBerg et al. (2014) | 12.56 | ± 0.46 | | |
| HD 140283 | G vs. G_{BP-G} | 14.02 | ± 1.27 | 14.13 | ± 1.3 |
| | G vs. $G-G_{RP}$ | 14.7 | ± 1.17 | 15.24 | ± 1.56 |
| | G vs. $G_{BP-G_{RP}}$ | 14.51 | ± 1.29 | 14.71 | ± 1.44 |
| | average | 14.41 | ± 0.65 | 14.69 | ± 1.03 |
| | VandenBerg et al. (2014) | 14.27 | ± 0.38 | | |
| | Bond et al. (2013) | 14.46 | ± 0.31 | | |

Table 9. Age derived for [VandenBerg et al. \(2014\)](#) stars.

| isochrone | filter | average age | error | weighted average age | error |
|--------------|-------------|-------------|-----------|----------------------|-----------|
| | | Gyr | Gyr | Gyr | Gyr |
| Padova | G vs. BP-G | 13.6 | ± 1.3 | 13.7 | ± 1.1 |
| | G vs. G-RP | 13.9 | ± 1.4 | 14.1 | ± 1.2 |
| | G vs. BP-RP | 13.8 | ± 1.3 | 13.9 | ± 1.1 |
| | average | 13.7 | ± 0.5 | 13.9 | ± 0.5 |
| BaSTI | G vs. BP-G | 13.4 | ± 0.7 | 13.5 | ± 0.7 |
| | G vs. G-RP | 13.6 | ± 0.7 | 13.9 | ± 0.7 |
| | G vs. BP-RP | 13.5 | ± 0.8 | 13.7 | ± 0.7 |
| | average | 13.5 | ± 0.4 | 13.7 | ± 0.4 |
| Padova+BaSTI | average | 13.8 | ± 0.3 | 14.1 | ± 0.3 |

Table 10. Average age of our stars

of ± 0.05 mag at the MS turnoff). The comparison between the two different sets of isochrones we use and our age determination of the three reference globular clusters suggest that 0.5 Gyr is a good estimation for our systematic error.

9.5. Age metallicity relation

The age metallicity relation (AMR) from G vs. G_{BP-G} , G vs. $G-G_{RP}$, G vs. $G_{BP-G_{RP}}$ diagrams is presented in Fig.15 and for average age in Fig.16 together with three ancient stars from [VandenBerg et al. \(2014\)](#) and three metal-poor GC: NGC 6397, M30, M92. The first column show result from Padova isochrones and the second column is from BaSTI. For the comparison we took the Milky Way Globular cluster AMR from [Dotter et al. \(2011\)](#) (in paper Fig.10) and [Cohen et al. \(2021\)](#) (in paper Fig.4) (dashed lines in Fig.15, 16). We can see that our stars extend the AMR to the lower metallicity side. On average metal-poor stars under investigation are older by about 0.8 Gyr than the main trends of the literature. And it is consistent with our results in Sec. ???. The average age for data set under consideration is 13.7 ± 0.4 Gyr (BaSTI, 28 stars), 13.9 ± 0.5 Gyr (Padova, 17) and 14.1 ± 0.3 Gyr (from BaSTI and Padova, 17 stars). Moreover for metallicity between $-2.7 - -2.0$ dex we have a minor population with relatively younger ages around 8 – 10 Gyr. It can be an indication of two different populations or two epochs of star formation.

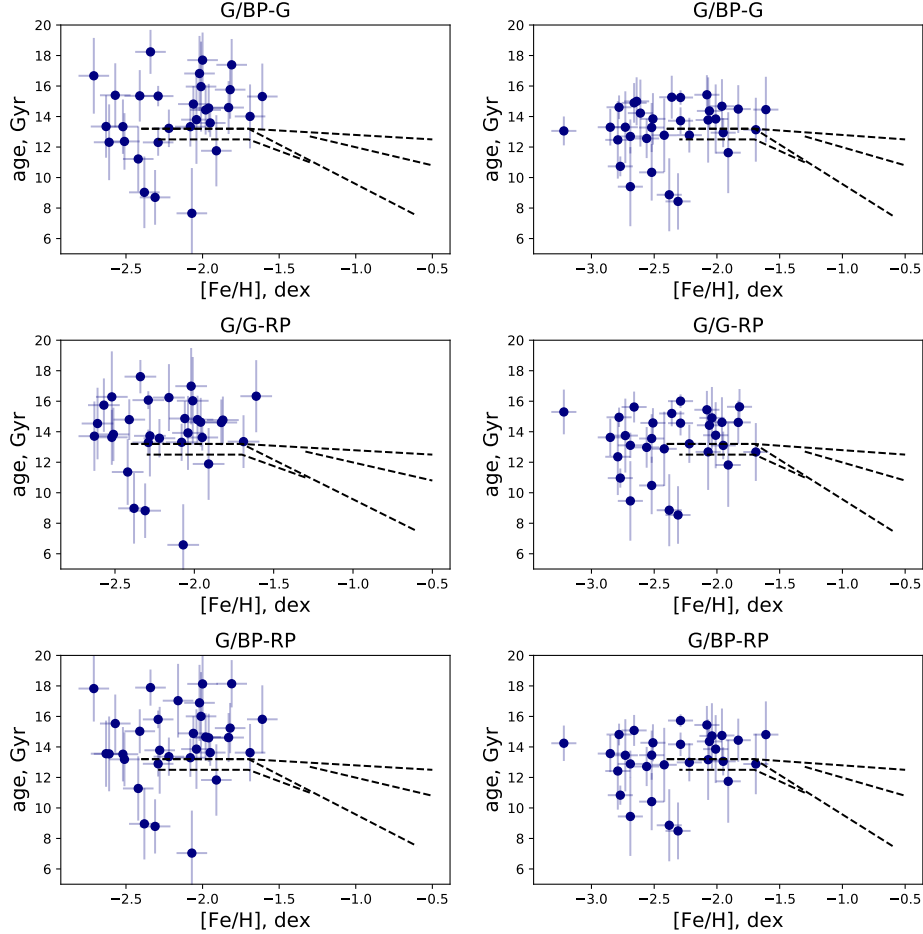


Figure 15. Age metallicity relation for ages from G vs. G_{BP-G} , G vs. G_{G-RP} , G vs. $G_{BP-G_{RP}}$ diagrams. *First column:* ages are from Padova isochrones, *second column:* from BaSTI.

10. CONCLUSION

In this study, we derived the age of 28 metal-poor stars (Tab.6). The average age from Padova isochrones is 13.9 ± 0.5 Gyr, from BaSTI - 13.7 ± 0.4 Gyr and for star with both determination it is of 14.1 ± 0.3 Gyr (internal errors only). Our estimate for the additional systematic error is around 0.5 Gyr.

Age was derived by automatic isochrone CMD fitting using Gaia DR3 photometry and the most updated parameters for distance and reddening. We considered also B,V photometry. Distance was chosen among four sources: Gaia DR3 (Gaia Collaboration (2021)), Gaia DR3 corrected by Lindegren et al. (2021), Bailer-Jones et al. (2021) and Queiroz et al. (2019) (StarHorse). Gaia DR3 parallaxes showed the best results in terms of CMD dispersion. We ascribe this result to the relative brightness of our stars. The best reddening estimate was obtained by combining two reddening maps Green et al. (2018) and Lallement et al. (2018) extended by Montalto et al. (2021).

We used two sets of isochrones, Padova and BaSTI. Padova isochrones produce on average 0.5 Gyr older age than BaSTI isochrones. Age determination can depend also on the detailed chemical composition of the stars. The enhancement of α -elements, C, N, O, and Ne can significantly affects the opacity of metal-poor stars and changes the continuum emission. The strongest effect is in the Johnson B filter (Fig.8). The effect is marginally present also in Gaia filters but, due to their width, it is much less prominent. We suggest that, in order to improve the age determination, specific isochrones should be computed for the chemical composition of each star.

In order to minimise the chemical composition effect in this work we used 3 different filter combinations of Gaia filters: G vs. G_{BP-G} , G vs. G_{G-RP} , G vs. $G_{BP-G_{RP}}$. We found that the age difference from one combination to the other is about 0.2 Gyr or less, smaller than the total uncertainty of the age determination method (more than 0.5 Gyr).

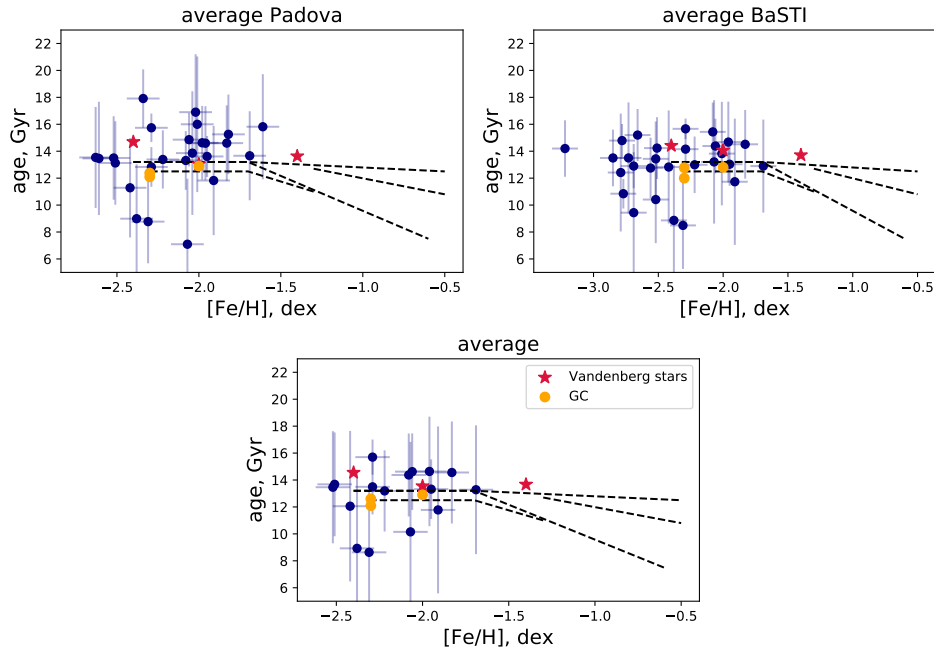


Figure 16. Average age metallicity relation for Padova (*left top*), BaSTI (*right top*) and Padova+BaSTI averaged together (*bottom*). Red stars are VandenBerg et al. (2014) targets. Yellow dots are three GC: NGC 6397, M 30, M92.

We checked our results against the three most metal-poor GC: NGC 6397, M 30, M 92. GC’s ages derived by our automatic isochrone fitting technique are in good agreement with ages derived by other authors (Correnti et al. (2018) (NGC 6397), Kains et al. (2013) (M 30), VandenBerg et al. (2016) (M 92)). Moreover, our set of very metal-poor stars on average is older than the most metal-poor GC by about 1 Gyr.

Additionally, we compared our results with the ages of three nearby ancient halo sub-giants (VandenBerg et al. (2014)). We found that our ages coincide within the uncertainties with the VandenBerg et al. (2014) and Bond et al. (2013) ages. Results are summarized in Tab.9.

Finally, we studied the age metallicity relation in its very metal-poor tail. The trend is almost horizontal, but our stars are on average older than mean locus found by other authors (Dotter et al. (2011), Cohen et al. (2021)) by about 0.8 Gyr. The interesting fact is that we found a group of very metal-poor stars with significantly young ages of 8 – 10 Gyr. The age of these stars can be a signature of two different populations or two epochs of star formation.

Our future plans include:

- Extending our data set for the new available samples of metal-poor and very metal-poor stars (Li et al. (2022), Xu et al. (2022), Lucey et al. (2022)).
- Assessing the origin of these stars through the detailed analysis of their kinematics and chemical composition.

The comments of an anonymous referee have been much appreciated. AP acknowledges the Ulisse program of Padova University which allowed her to spend a period at Concepcion University, where part of this works has been done. SV gratefully acknowledges the support provided by Fondecyt regular n. 1220264 and by the ANID BASAL projects ACE210002 and FB210003.

REFERENCES

- Ade, P. A. R., Aghanim, N., Armitage-Caplan, C., et al. 2014, *Astronomy & Astrophysics*, 571, A16
- Bailer-Jones, C. A. L., Rybizki, J., Fousneau, M., Demleitner, M., & Andrae, R. 2021, *AJ*, 161, 147

- Barklem, P. S., Christlieb, N., Beers, T. C., et al. 2005, *A&A*, 439, 129
- Bennett, C. L., Larson, D., Weiland, J. L., et al. 2013, *The Astrophysical Journal Supplement Series*, 208, 20
- Bird, J. C., Kazantzidis, S., & Weinberg, D. H. 2012, *MNRAS*, 420, 913
- Bonaca, A., Conroy, C., Cargile, P. A., et al. 2020, *ApJL*, 897, L18
- Bond, H. E., Nelan, E. P., VandenBerg, D. A., Schaefer, G. H., & Harmer, D. 2013, *ApJL*, 765, L12
- Bonfanti, A., Ortolani, S., Piotto, G., & Nascimbeni, V. 2015, *A&A*, 575, A18
- Bromm, V., & Larson, R. B. 2004, *ARA&A*, 42, 79
- Carter, C., Conroy, C., Zaritsky, D., et al. 2021, *ApJ*, 908, 208
- Cayrel, R., Depagne, E., Spite, M., et al. 2004, *A&A*, 416, 1117
- Christlieb, N., Beers, T. C., Barklem, P. S., et al. 2004, *A&A*, 428, 1027
- Cohen, R. E., Bellini, A., Casagrande, L., et al. 2021, *AJ*, 162, 228
- Correnti, M., Gennaro, M., Kalirai, J. S., Cohen, R. E., & Brown, T. M. 2018, *ApJ*, 864, 147
- Dotter, A., Sarajedini, A., & Anderson, J. 2011, *ApJ*, 738, 74
- El-Badry, K., Rix, H.-W., & Heintz, T. M. 2021, *MNRAS*, arXiv:2101.05282
- Feillet, D. K., Bovy, J., Holtzman, J., et al. 2018, *MNRAS*, 477, 2326
- Frebel, A., & Norris, J. E. 2015, *ARA&A*, 53, 631
- Gaia Collaboration. 2021, *A&A*, 649, A1
- Gaia Collaboration, Gaia Collaboration, De Ridder, J., et al. 2022, arXiv e-prints, arXiv:2206.06075
- Green, G. M., Schlafly, E. F., Finkbeiner, D., et al. 2018, *MNRAS*, 478, 651
- Grenon, M. 1972, in *IAU Colloq. 17: Age des Etoiles*, ed. G. Cayrel de Strobel & A. M. Delplace, 55
- Grenon, M. 1989, *Ap&SS*, 156, 29
- Hidalgo, S. L., Pietrinferni, A., Cassisi, S., et al. 2018, *ApJ*, 856, 125
- Kains, N., Bramich, D. M., Arellano Ferro, A., et al. 2013, *A&A*, 555, A36
- Lallement, R., Capitanio, L., Ruiz-Dern, L., et al. 2018, *A&A*, 616, A132
- Li, H., Aoki, W., Matsuno, T., et al. 2022, *ApJ*, 931, 147
- Limberg, G., Santucci, R. M., Rossi, S., et al. 2021, *ApJ*, 913, 11
- Lindgren, L., Bastian, U., Biermann, M., et al. 2021, *A&A*, 649, A4
- Lucey, M., Al Kharusi, N., Hawkins, K., et al. 2022, arXiv e-prints, arXiv:2206.08299
- Montalto, M., Piotto, G., Marrese, P. M., et al. 2021, *A&A*, 653, A98
- Queiroz, A. B. A., Anders, F., Chiappini, C., et al. 2019, arXiv e-prints, arXiv:1912.09778
- Quillen, A. C., Minchev, I., Bland-Hawthorn, J., & Haywood, M. 2009, *MNRAS*, 397, 1599
- Ritter, J. S., Safrank-Shrader, C., Gnat, O., Milosavljević, M., & Bromm, V. 2012, *ApJ*, 761, 56
- Roškar, R., Debattista, V. P., Stinson, G. S., et al. 2008, *ApJL*, 675, L65
- Safrank-Shrader, C., Milosavljevic, M., & Bromm, V. 2014, *MNRAS*, 440, L76
- Salaris, M., Chieffi, A., & Straniero, O. 1993, *ApJ*, 414, 580
- Schlafly, E. F., & Finkbeiner, D. P. 2011, *ApJ*, 737, 103
- Schlaufman, K. C., & Casey, A. R. 2014, *ApJ*, 797, 13
- Schlegel, D. J., Finkbeiner, D. P., & Davis, M. 1998, *ApJ*, 500, 525
- Sellwood, J. A., & Binney, J. J. 2002, *MNRAS*, 336, 785
- Twarog, B. A. 1980, *ApJ*, 242, 242
- VandenBerg, D. A., Bond, H. E., Nelan, E. P., et al. 2014, *ApJ*, 792, 110
- VandenBerg, D. A., Denissenkov, P. A., & Catelan, M. 2016, *ApJ*, 827, 2
- Xu, S., Yuan, H., Zhang, R., et al. 2022, arXiv e-prints, arXiv:2207.02371